The origin of the current-driven breakdown in vanadium oxides: thermal vs electronic

I. Valmianski[1], P. Y. Wang[1], S. Wang[1,2], Juan Gabriel Ramirez[3], S. Guénon[4], Ivan K. Schuller[1]

[1] *Department of Physics and Center for Advanced Nanoscience, University of California San Diego, La Jolla, California 92093, USA*

[2] *Materials Science and Engineering Program, University of California, San Diego*

[3] *Department of Physics, Universidad de los Andes, Bogotá 111711, Colombia*

[4]*Physikalisches Institut-Nano Atomoptics, Tubingen, Germany*

We report the existence of two competing mechanisms in the current-driven electrical breakdown of vanadium sesquioxide (V_2O_3) and vanadium dioxide (VO_2) nanodevices. Our experiments and simulations show that the competition between a purely-electronic mechanism (PE) and an electro-thermal (ET) mechanism, suppressed in nanoscale devices, explains the current driven insulator-to-metal phase transition (IMT). We find that the relative contribution of PE and ET effects is dictated by thermal coupling and resistivity, a discovery which disambiguates a long-standing controversy surrounding the physical nature of the current-driven IMT in vanadium oxides. Furthermore, we show that the electro-thermally driven IMT occurs through a nanoscopic surface-confined filament. This nano-confined filament has a very large thermal gradient, thus generating a large Seebeck-effect electric field.

I. INTRODUCTION

Vanadium dioxide (VO_2) and vanadium sesquioxide (V_2O_3) are strongly electron-correlated materials that exhibit insulator-to-metal transitions (IMT) in equilibrium or non-equilibrium conditions [1,2]. In equilibrium, the IMT can be driven by temperature or pressure [3] and has

been studied extensively. Recently, the IMT in non-equilibrium conditions, as in the current driven transition, has attracted special attention due to extremely fast changes in electronic properties which generate strong electrical [4–10], optical [11–13], and magnetic responses [14–17]. Previous X-ray studies have demonstrated the existence of "hidden" non-equilibrium states in the photo-excited IMT of V_2O_3 [2] as well as the separation of electric and structural transitions in VO_2 in the presence of electric fields [18]. The current driven IMT potentially offers a novel road to access these non-equilibrium states in future devices. However, the current driven transition remains controversial since it can be triggered by purely electronic contributions [19,20] or by pure Joule heating effects [4,8]. Moreover, ultrafast studies show that purely electronic contributions and pure Joule heating may remain intertwined, even on the picosecond timescale [21].

To address the above-mentioned controversy, we compared the current driven IMTs of VO_2 and V_2O_3 nanodevices. We performed experimental measurements that reveal fundamental differences in the overall behavior of the IMT between the two materials. We then developed a three-dimensional model which elucidates the mechanisms underlying the current-driven IMT. We find that the electro thermal(ET) mechanism is supressed at the nanoscale and that the combination of both a purely-electronic (PE) and an electro-thermal (ET) model is necessary to explain the experimental results. The discovery of the competition between these two mechanisms (PE vs. ET) resolves a long-standing controversy surrounding the current-driven IMTs of VO_2 and V_2O_3. Furthermore, the length scales of these two mechanisms can be leveraged for the development of novel devices.

II. EXPERIMENTAL

To study the current driven electrical breakdown, we fabricated VO_2 and V_2O_3 nanodevices with identical geometries (see insets Fig 1). The geometry of these nanodevices was chosen to minimize electrothermal heating and localize filament formation [4,8].100 nm V_2O_3 and VO_2 thin films were grown using magnetron sputter deposition as described in ref [22]. The film structure was determined using X-ray diffraction (Rigaku Smartlab Diffractometer), which showed that the films were highly textured in both out-of-plane and in-plane directions. The devices were fabricated on the films using a three-step lithographic process. First, 20 µm x 50 µm vanadium oxide islands were defined with negative-resist photolithography. Vanadium oxide outside of the islands was etched with reactive ion etching with Oxford Instruments P80 RIE system. The etching was performed for 2 minutes under 40 mTorr pressure with 50 sccm Cl_2 and 10 sccm Ar flow at 200 W. In the second lithographic step, triangular electrodes were defined using e-beam lithographic system Raith50 with 950 PMMA C4 positive resist. Exposure doses ranged between 270 and 330 µC/cm^2 to adjust the gap size to the desired value of 140 x 200 nm. The electrodes were deposited by e-beam physical vapor deposition with a 20 nm of V adhesion layer followed by an 80 nm Au layer at a rate of 1 A/s. Finally, positive resist (S1818) photo-lithography was used to define larger electrodes and connection pads. The devices were inspected by scanning electron microscopy (SEM). An example of the device is presented in the inset of Fig. 1a.

Electrical measurements were performed in a two-probe configuration using Keithley 6221A current source and Keithely 2181A nanovoltmeter in a closed cycle cryostat. Two types of electrical measurements were performed. Resistance-temperature characteristic was measured with a fixed current of 100 nA, which is significantly below the threshold needed to induce a metal-insulator transition. Current-voltage characteristic was measured by slowly ramping up the

current (1 μA/s) to 200 μA while keeping the substrate temperature fixed. This measurement was performed ten times at each temperature with a sampling rate of 5 Hz to ensure reproducibility. R-T curves were taken at a temperature ramp rate of 1 K/min.

III. RESULTS AND DISCUSSION

The temperature dependent resistivity of both types of devices is shown in Figs. 1a and 1b. Both devices show three and a half order of magnitude change in resistance with temperature. The VO_2 transition temperatures were 332 K and 336 K for the cooling and heating branches respectively, similar to bulk [1], while the V_2O_3 transition temperatures were slightly elevated at 160 K and 166 K [3]. The R-T curves are reproducible and very sensitive to the device temperature. We have shown earlier [4], by using a local submicron thermometer, that the resistivity is a reliable indicator of the local temperature. This property allows us to use the device resistance outside the thermal hysteresis, when the current and temperature distributions are homogenous, as a measure of local temperature.

The current-voltage (IV) characteristics as a function of substrate temperature are shown in Fig. 1c for V_2O_3 and in Fig. 1d for VO_2. The region of negative differential resistance corresponds to a current driven IMT. The IV curve is smooth before the transition and is characterized by multiple jumps as the device undergoes the IMT due to an avalanche-like behavior [23]. The initial large jump results from the formation of a conducting filament connecting the two electrodes [8]. The change in device temperature below the IMT as a function of dissipated power (Fig 2a, b) is extracted from the R-T curves (Fig. 1) and the IV product respectively.

In VO_2 (Fig 2a), the temperature change ΔT depends linearly on the dissipated power P, requiring higher dissipated power for lower temperatures. This is in agreement with previous studies of microscopic VO_2 devices [4] and can be explained as a combination of Joule heating together

with Fourier's Law of Conduction, labeled here as the "electro-thermal" (ET) model. However, in V_2O_3 (Fig 2b), ΔT changes sublinearly as a function of P at much lower power than in VO_2. Moreover, the P needed to induce the IMT *decreases* with decreasing base temperatures. This is inconsistent with a purely ET model and indicates the presence of electronic contributions [4,8]. In Fig 2c, we compare the effective breakdown electric field with the square root of the breakdown fluence [24] in an independently measured optically driven V_2O_3 transition. The two normalized curves agree, suggesting that the field dependence of the current driven V_2O_3 transition is similar to the optically-driven transition.

To model our devices, we performed steady state finite element method (FEM) simulations in COMSOL Multiphysics. The simulations were calculated under the same conditions as experiments with dimensions of the simulated device reflecting that of the fabricated device. The model incorporates the Joule heating module which couples electrodynamics and heat transfer physics (ET) and uses our experimental data for resistivity extracted from equilibrium R vs T curves as well as literature values for other material parameters [25–29]. Inspired by the linear relationship between base temperature and normalized breakdown electric field for V_2O_3 (Fig. 2c), we used the Domain ODE module to implement an effective temperature (PE) model $T_{eff} = T_{loc} + \alpha E_{loc}$ where T_{loc} is the local temperature, E_{loc} is the local electric field, and α is a fitting constant. The local temperature and electric field are computed in the FEM model, and the parameter α is fitted using the experimental breakdown electric field. Calculations were made for base temperatures of 310 K, 320 K, and 330 K for VO_2 devices and 120 K, 135K, and 150 K for V_2O_3 devices.

Simulated temperature and current density profiles for VO_2 at 310 K base temperature are presented in Fig. 3. Figure 3a shows the simulated IV characteristic with dashed lines indicating

the applied current at which the (top and side view) current densities and temperatures are plotted in Fig. 3(b-i). The current distribution is relatively homogenous throughout the bridge before the filament formation. Once the critical current is reached, a filament spontaneously forms. This causes a drastic drop in the current density outside the filament and a three orders of magnitude increase in the current density inside the filament. The filament is largely confined to the surface (Fig 3h, i), penetrating less than 10 nm deep (with a similar width). The small filament size is due to strong cooling at the substrate and contacts. Similar simulation results were found for other base temperatures in VO_2.

Using the results of our simulations, we calculated IV characteristics, ΔT vs P, and breakdown voltage vs substrate temperature (Fig. 4). The simulations are in excellent qualitative agreement with the experiments. The ΔT vs P in Fig 4b is linear up to 60 μW and then becomes superlinear. However, the 330 K experimental curve, does not fall on top the 320 K and 310 K curves. This is likely caused by the presence of defects which our simulation does not address. Fig. 4c shows qualitative agreement between experiment and simulation in the breakdown power as a function of substrate temperature. This suggests that the current driven transition in VO_2 can be explained by a purely ET model.

Fig 4d,e show the simulated IV characteristics and ΔT vs P for a V_2O_3 device. A purely ET model cannot reproduce our V_2O_3 results (see Fig. 1 of the Supplemental Material [30]); however, the addition of an electric field dependent effective temperature model (ET and PE) reproduces the experimental results well. Fig. 4f shows that the breakdown power in the simulation and the experiment increases with increasing base temperature. This could not occur in a simple ET process in which the temperature increase should be proportional to the dissipated power. We believe that using grain switching instead of our continuous conductivity

approximation may improve the qualitative agreement but is very computationally expensive. Another potentially fruitful approach is to consider the current driven changes in the magnetic ordering of V_2O_3. Recent work on Ca_2RuO_4, which has a similar to V_2O_3 insulating state, reveals a current driven IMT driven by the melting of the antiferromagnetic Mott ordering [31].

The difference between the VO_2 and V_2O_3 devices is due to competition between electric field induced and Joule heating induced switching (PE vs ET). Because V_2O_3 has an order of magnitude larger base resistance, the power dissipated by Joule heating is an order of magnitude less than in VO_2 for the same electric field. Furthermore, the discrepancy between our study and previous V_2O_3 device experiments [8,32] can be explained by geometry and resistivity. Since thermal dissipation scales with the square of device size while heat production scales with the cube of device size, Joule heating plays a smaller role for smaller devices. Moreover, resistivity in the insulating state controls the relative contribution of ET and PE mechanisms. This explains why the transition appeared to be purely Joule heating induced (ET) in previous V_2O_3 device experiments [8,32] whereas PE contributions are strongly enhanced in our nanodevice.

The large thermal gradients (Fig. 3b, d) in the filaments generate large thermopower electric fields. Fig. 5 shows the simulated thermopower (Seebeck) electric field as a function of current for a VO_2 device. The temperature distribution is uniform before the filament is established. However, once the filament is formed, the vanadium oxide outside the filament cools down while the filament itself is strongly heated (Fig 3). In the out-of-plane direction, using the bulk VO_2 Seebeck coefficient ~150 μV/K [33] implies a thermopower electric field as large as 1.8 kV/cm, which is about 2% of the 90 kV/cm driving field. This magnitude of the induced field is atypical for nanodevices, with the only comparable systems being non-local spin valves and

carbon nanotubes [33–36]. Future research is needed to experimentally verify the large implied Seebeck fields.

IV. CONCLUSION

In summary, we compared the current driven IMT in VO_2 and V_2O_3 nanodevices at temperatures as low as 30 K below IMT and discovered competing breakdown mechanisms (PE vs ET). We found that the VO_2 device behavior can be explained using a purely electro-thermal (ET) FEM model and that the transition occurs through the formation of a nanoscopic filament. The conducting filament is mostly confined to the surface and has a very large temperature gradient (Fig 5). This large temperature gradient generates a large thermopower electric field which is interesting for thermopower applications (induced electric field of about 10^3 V/cm) as well as caloritronics. Conversely, experimental verification of a large thermopower electric field can confirm a nanoscopic filamentary ET transition. In V_2O_3, the transition occurs through a combination of purely electronic and electro-thermal (PE and ET) contributions. Because the thermal coupling to the environment is larger for smaller devices, thermal effects are supressed and become less prominent than the purely electronic contributions. Moreover, the larger resistivity of V_2O_3 results in smaller dissipated power (decreased ET contributions) and allows for the application of larger electric fields (increased PE contributions). This discovery opens a new avenue for searching for an electric field induced IMT in VO_2 and similar materials by tuning the relative contributions of each mechanism. Furthermore, our finding of an electric field induced transition in V_2O_3 can be leveraged for the design of novel functional electronic and spintronic devices.

References

[1]   M. Imada, A. Fujimori, and Y. Tokura, Rev. Mod. Phys. **70**, 1039 (1998).

[2]   A. Singer, J. G. Ramirez, I. Valmianski, D. Cela, N. Hua, R. Kukreja, J. Wingert, O. Kovalchuk, J. M. Glownia, M. Sikorski, M. Chollet, M. Holt, I. K. Schuller, and O. G. Shpyrko, Phys. Rev. Lett. **120**, 207601 (2018).

[3]   D. B. McWhan, A. Menth, J. P. Remeika, W. F. Brinkman, and T. M. Rice, Phys. Rev. B **7**, 1920 (1973).

[4]   A. Zimmers, L. Aigouy, M. Mortier, A. Sharoni, S. Wang, K. G. West, J. G. Ramirez, and I. K. Schuller, Phys. Rev. Lett. **110**, 56601 (2013).

[5]   I. P. Radu, B. Govoreanu, S. Mertens, X. Shi, M. Cantoro, M. Schaekers, M. Jurczak, S. De Gendt, a Stesmans, J. a Kittl, M. Heyns, and K. Martens, Nanotechnology **26**, 165202 (2015).

[6]   P. Markov, R. E. Marvel, H. J. Conley, K. J. Miller, R. F. Haglund, and S. M. Weiss, ACS Photonics **2**, 1175 (2015).

[7]   B. A. Kruger, A. Joushaghani, and J. K. S. Poon, Opt. Express **20**, 23598 (2012).

[8]   S. Guénon, S. Scharinger, S. Wang, J. G. Ramírez, D. Koelle, R. Kleiner, and I. K. Schuller, Europhys. Lett. **101**, 57003 (2013).

[9]   H.-T. Kim, B.-J. Kim, S. Choi, B.-G. Chae, Y. W. Lee, T. Driscoll, M. M. Qazilbash, and D. N. Basov, J. Appl. Phys. **107**, 23702 (2010).

[10]   T. Driscoll, J. Quinn, M. Di Ventra, D. N. Basov, G. Seo, Y.-W. Lee, H.-T. Kim, and D. R. Smith, Phys. Rev. B **86**, 94203 (2012).

[11]   M. M. Qazilbash, A. A. Schafgans, K. S. Burch, S. J. Yun, B. G. Chae, B. J. Kim, H. T. Kim, and D. N. Basov, Phys. Rev. B **77**, 115121 (2008).

[12]   O. V. Misochko, M. Tani, K. Sakai, K. Kisoda, S. Nakashima, V. N. Andreev, and F. A. Chudnovsky, Phys. Rev. B **58**, 12789 (1998).

[13]   F. Béteille and J. Livage, J. Sol-Gel Sci. Technol. **921**, 915 (1998).

[14]   J. de la Venta, S. Wang, J. G. Ramirez, and I. K. Schuller, Appl. Phys. Lett. **102**, 122404 (2013).

[15]   J. De La Venta, S. Wang, T. Saerbeck, J. G. Ramírez, I. Valmianski, and I. K. Schuller, Appl. Phys. Lett. **104**, (2014).

[16]   T. Saerbeck, J. de la Venta, S. Wang, J. G. Ramírez, M. Erekhinsky, I. Valmianski, and I. K. Schuller, J. Mater. Res. **29**, 2353 (2014).

[17]   M. Erekhinsky, J. De La Venta, and I. K. Schuller, J. Appl. Phys. **114**, (2013).

[18]   B.-J. Kim, Y. W. Lee, S. Choi, J.-W. Lim, S. J. Yun, H.-T. Kim, T.-J. Shin, and H.-S. Yun, Phys. Rev. B **77**, 235401 (2008).

[19]   T. Oka, R. Arita, and H. Aoki, Phys. Rev. Lett. **91**, (2003).

[20]   V. Guiot, L. Cario, E. Janod, B. Corraze, V. Ta Phuoc, M. Rozenberg, P. Stoliar, T. Cren, and D. Roditchev, Nat. Commun. **4**, (2013).

[21]   M. Liu, H. Y. Hwang, H. Tao, A. C. Strikwerda, K. Fan, G. R. Keiser, A. J. Sternbach, K. G. West, S. Kittiwatanakul, J. Lu, S. A. Wolf, F. G. Omenetto, X. Zhang, K. A. Nelson,

and R. D. Averitt, Nature **487**, 345 (2012).

[22] M. K. Stewart, D. Brownstead, S. Wang, K. G. West, J. G. Ramirez, M. M. Qazilbash, N. B. Perkins, I. K. Schuller, and D. N. Basov, Phys. Rev. B - Condens. Matter Mater. Phys. **85**, 205113 (2012).

[23] S. Wang, J. G. Ramírez, and I. K. Schuller, Phys. Rev. B - Condens. Matter Mater. Phys. **92**, 85150 (2015).

[24] E. Abreu, S. Wang, J. G. Ramírez, M. Liu, J. Zhang, K. Geng, I. K. Schuller, and R. D. Averitt, Phys. Rev. B **92**, 085130 (2015).

[25] H. Kizuka, T. Yagi, J. Jia, Y. Yamashita, S. Nakamura, N. Taketoshi, and Y. Shigesato, Jpn. J. Appl. Phys. **54**, (2015).

[26] V. N. Andreev, F. A. Chudnovskii, A. V Petrov, and E. I. Terukov, Phys. Status Solidi **48**, K153 (1978).

[27] R. A. Matula, J. Phys. Chem. Ref. Data **8**, 1147 (1979).

[28] E. R. Dobrovinskaya, L. A. Lytvynov, and V. Pishchik, in *Sapphire Mater. Manuf. Appl.* (Springer US, Boston, MA, 2009), pp. 55–176.

[29] C. Y. Ho, R. W. Powell, and P. E. Liley, J. Phys. Chem. Ref. Data **1**, 279 (1972).

[30] See Supplemental Material at [URL will be inserted by publisher] for observables obtained from a purely ET model for our V_2O_3 nanodevice, which includes Refs. [4, 8, 20 ,23, 32, 37-41]

[31] C. Sow, S. Yonezawa, S. Kitamura, T. Oka, K. Kuroki, F. Nakamura, and Y. Maeno, Science (80-.). **358**, 1084 (2017).

[32] J. S. Brockman, L. Gao, B. Hughes, C. T. Rettner, M. G. Samant, K. P. Roche, and S. P. P. Stuart, Nat. Nanotechnol. **9**, 453 (2014).

[33]   J. Cao, W. Fan, H. Zheng, and J. Wu, Nano Lett. **9**, 4001 (2009).

[34]   G. E. W. Bauer, E. Saitoh, and B. J. van Wees, Nat Mater **11**, 391 (2012).

[35]   D. H. and T. U. and Y. N. and H. K. and Y. M. and T. Y. and T. S. and K. H. and Y. Maniwa, Appl. Phys. Express **9**, 25102 (2016).

[36]   F. Casanova, A. Sharoni, M. Erekhinsky, and I. K. Schuller, Phys. Rev. B **79**, 184415 (2009).

[37]   J. A. Pelesko and D. H. Bernstein, in *Model. Mems Nems* (CRC press, Boca Raton, 2003), pp. 91–123.

[38]   A. S. McLeod, E. van Heumen, J. G. Ramirez, S. Wang, T. Saerbeck, S. Guenon, M. Goldflam, L. Anderegg, P. Kelly, A. Mueller, M. K. Liu, I. K. Schuller, and D. N. Basov, Nat. Phys. **13**, 80 (2016).

[39]   J. Etienne, T. Julien, C. Benoit, Q. Madec, S. Pablo, R. Marcelo, C. Tristan, R. Dimitri, P. V. Ta, B. Marie   Paule, and C. Laurent, Adv. Funct. Mater. **25**, 6287 (2015).

[40]   S. Pablo, C. Laurent, J. Etiene, C. Benoit, G. Catherine, S. Sabrina, G. Vincent, T. Julien, and R. Marcelo, Adv. Mater. **25**, 3222 (2013).

[41]   P. Stoliar, M. Rozenberg, E. Janod, B. Corraze, J. Tranchant, and L. Cario, Phys. Rev. B **90**, 45146 (2014).
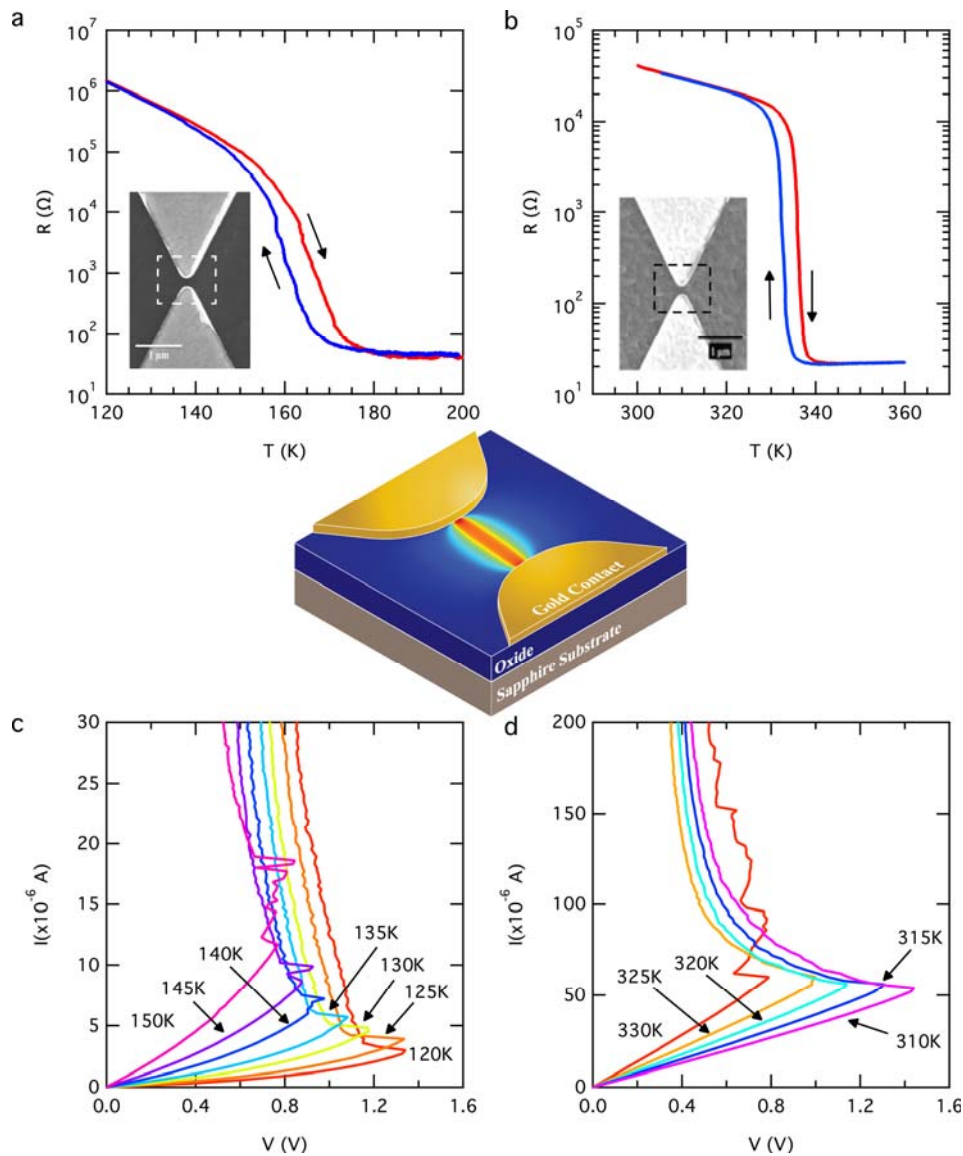
Figure 1. (a,b) Resistivity-temperature characteristic of a typical (a) V_2O_3 and (b) VO_2 device (SEM image in the inset, light is metallic electrode, dark is V_2O_3 and VO_2). Blue and red line signifies the cooling and heating branch, respectively. (c,d) I-V characteristics of the (c) V_2O_3 and (d) VO_2 devices. The substrate temperature is indicated for each device. Middle inset is 3D rendering of a device with a simulated temperature in between the electrodes after the current-driven transition occurs.
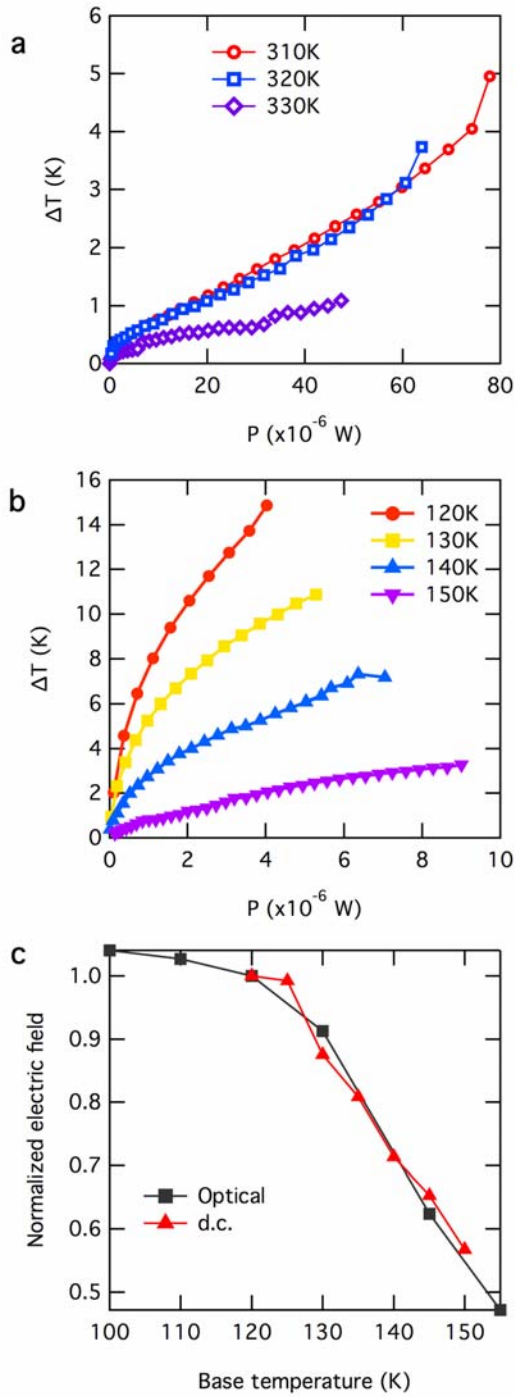
Figure 2. Change in device temperature as a function of applied power (IV product) for (a) VO_2 and (b) V_2O_3. (c) Comparison of the normalized breakdown electric field vs. substrate temperature for electrically and optically driven V_2O_3 transition.
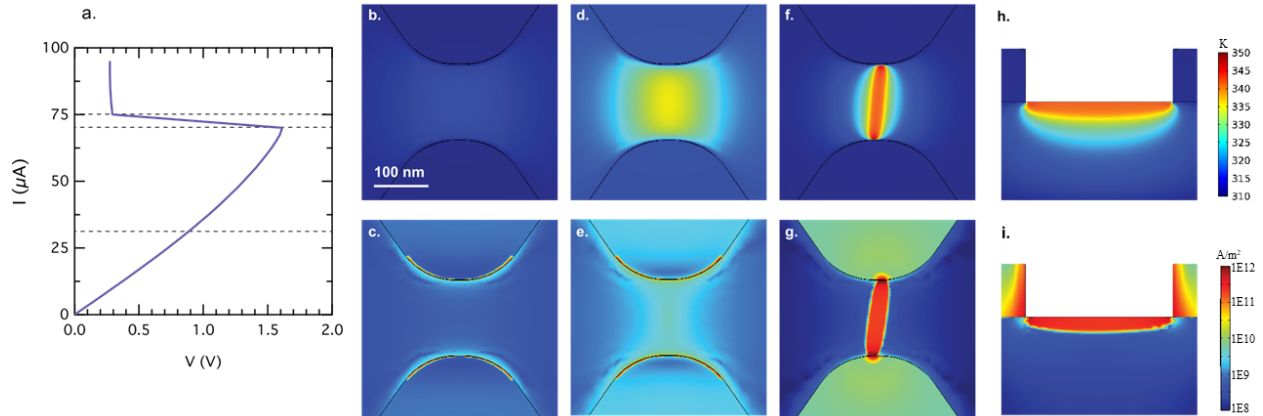
Figure 3. Steady state simulation of a VO$_2$ device with 310 K starting temperature at three different currents as indicated by the horizontal dashed lines in the simulated IV curve in (a). Top (Bottom) panel corresponds to temperature (current density) maps for (b,c) 30, (d,e) 70 and (f,g) 75 μA. Top down view of the surface (h) temperature distribution and (i) current density. The filament is not perfectly straight due to small symmetry breaking in the mesh.
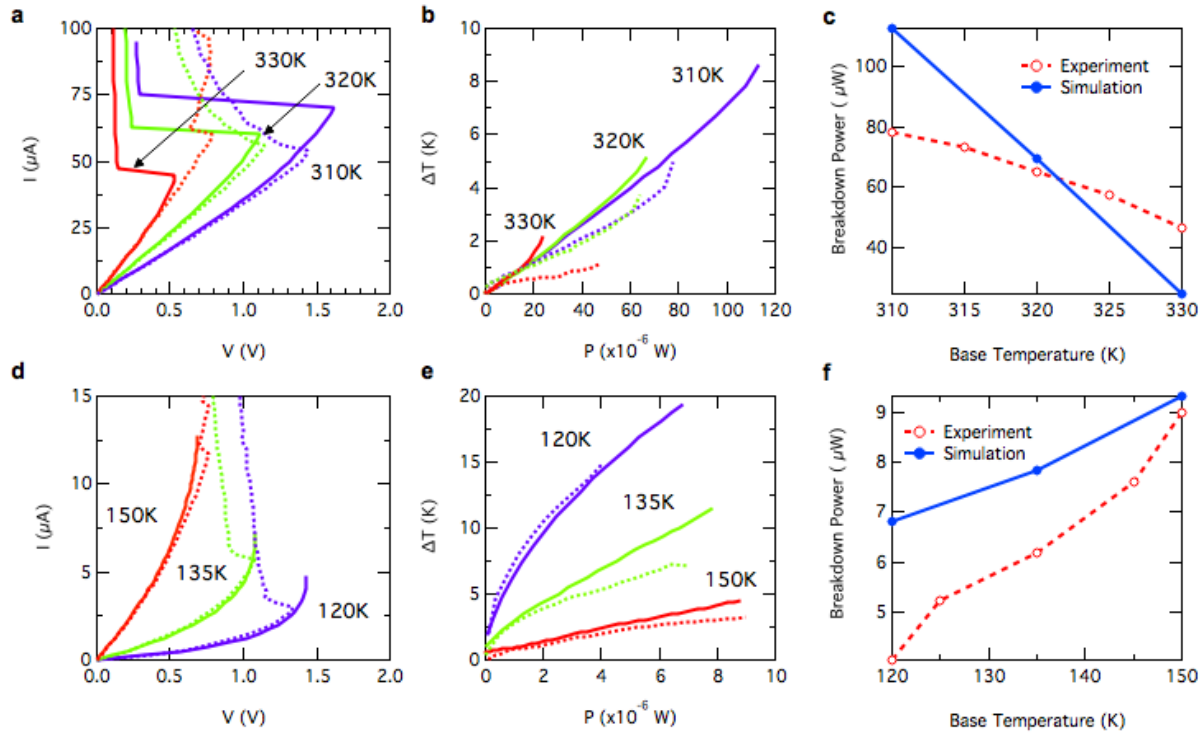
Figure 4. Observables obtained from the COMSOL simulation of VO_2 and V_2O_3 devices as a function of substrate temperature. Simulated VO_2 (a) I-V characteristic and (b) temperature - power characteristic. (c) Comparison of the simulation and experimental results for the IMT breakdown power. Simulated V_2O_3 (d) I-V characteristic and (e) temperature -power characteristic. (f) Comparison of the simulation (solid blue line) and experimental results (dashed red line) for the IMT breakdown power. Dashed lines correspond to experimental data.
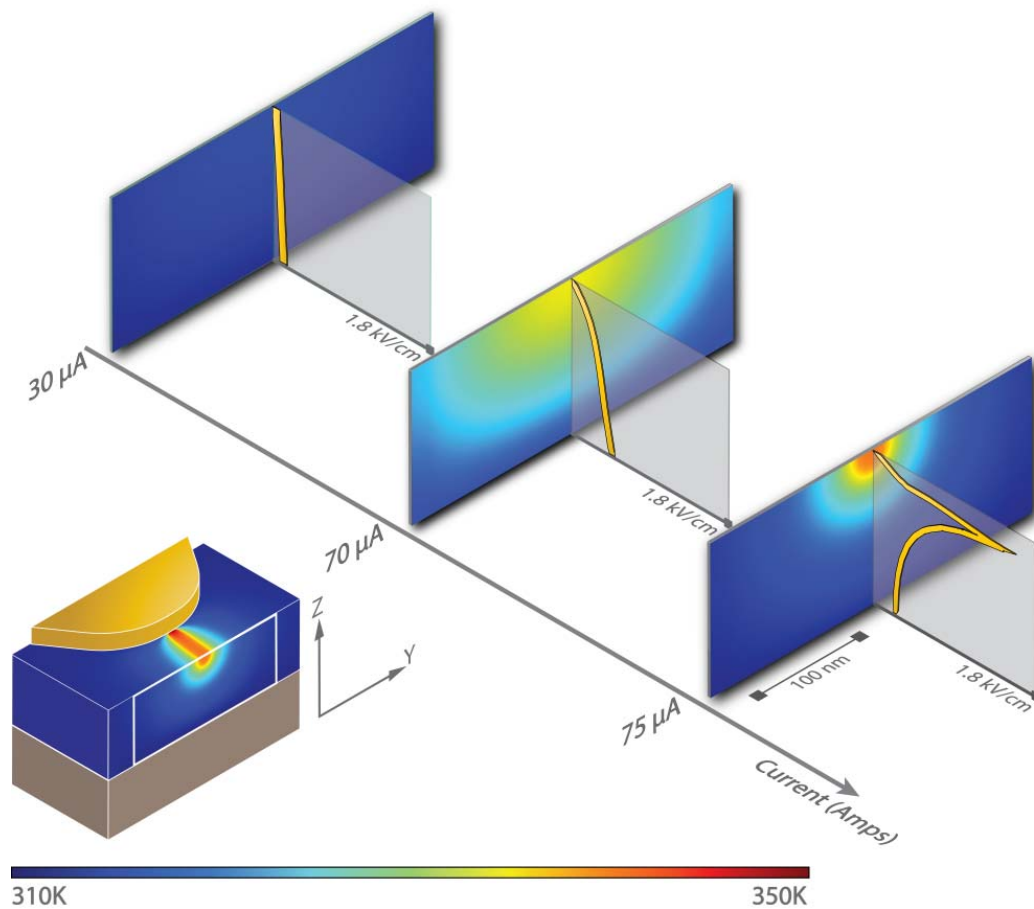
Figure 5. Seebeck electric field as a function of position in the filament at three applied currents (30 μA, 70 μA, and 75 μA). Inset shows the cross section of the filament for which the fields were calculated.